Reversing and nonreversing modulated Taylor-Couette flow at finite aspect ratio

Anthony J. Youd and Carlo F. Barenghi
Department of Mathematics, University of Newcastle upon Tyne, Newcastle upon Tyne, NE1 7RU, United Kingdom
(Received 3 May 2005; revised manuscript received 1 August 2005; published 29 November 2005)

Recent work on the Taylor-Couette problem in the infinite-cylinder approximation has revealed that, if the driving velocity of the inner cylinder is not steady but modulates in time, two classes of time-dependent flow exist: reversing flows and nonreversing flows. The latter are at first surprising, since the direction of rotation of the Taylor vortices is decoupled from the (driving) azimuthal flow. Since experiments are performed in cylinders of finite height, the natural question which we address in this paper is whether the Ekman circulation induced by the end walls suppresses the reversing-nonreversing effect. We find that the answer is negative—nonreversing flows are actually favoured—and we reveal a variety of new flow patterns including "side-by-side" vortices.

DOI: 10.1103/PhysRevE.72.056321 PACS number(s): 47.20.−k, 47.32.Cc

I. INTRODUCTION

The transition from azimuthal Couette flow to a cellular Taylor vortex flow pattern has long been recognized as a cornerstone of hydrodynamic stability theory. In recent papers [1,2] we have considered a variation of this classical problem (assuming the infinite-cylinder approximation), in which the inner cylinder's angular velocity is not steady but oscillates harmonically around zero mean according to

$$\Omega(t) = \Omega_a \cos(\omega t), \tag{1}$$

where Ω_a and ω are the dimensional amplitude and frequency, respectively, and the outer cylinder remains at rest. We have found that two classes of Taylor vortex flow exist. In the first class the direction of rotation of the Taylor vortex flow is the natural one which is induced by the direction of rotation of the azimuthal flow imposed by the inner cylinder, so it changes sign during each cycle; we called this class reversing Taylor vortex flow (RTVF)—see Fig. 1. In the second class, which occurs at sufficiently large amplitude and frequency of modulation, the Taylor vortices always rotate in the same direction, irrespective of the direction of the underlying azimuthal flow, thus keeping memory of the first cycle; we called this class nonreversing Taylor vortex flow (NRTVF)—see Fig. 2. At the same amplitude of modulation, the transition from RTVF to NRTVF takes place at a critical frequency ω. We also found the existence of reversing and nonreversing flows in the wavy-mode regime. Here, the nonreversing flow takes the form of a spiral mode. This same effect was also found by Zhang [3] in spherical geometry.

Our calculations were based on the usual approximation of infinite cylinders. However, the work of Benjamin [4,5], Benjamin and Mullin [6], Cliffe [7], Pfister *et al.* [8], Cliffe *et al.* [9], Mullin *et al.* [10], Furukawa *et al.* [11], and Lopez and Marques [12] has shown that end effects play a key role in selecting the steady cellular vortex pattern and that an important parameter of the problem is the aspect ratio Γ (the ratio of the height of the cylinders to the width of the gap). The existence of the ends gives rise to the so-called "anomalous" modes where the cells close to the ends have a direction of rotation which is apparently opposite to what is initially expected (radial outflow at the midplane where the centrifugal force is stronger and radial inflows near the cylinders' ends). The anomalous modes appear to have an outflow at the ends; closer inspection reveals the existence of small vortices in the corners near to the inner cylinder, but the name "anomalous" has not been changed and has remained in the literature to distinguish this remarkable flow pattern. In terms of bifurcation theory, anomalous modes are always disconnected from the primary two-cell flow; only one exception is known: as the aspect ratio is reduced such that the height of the cylinders is of the order of the gap between the cylinders, an anomalous one-cell state is found which is connected to the primary flow and can be realized by a quasistatic increase in the Reynolds number.

In the infinite-cylinder approximation and in relatively long cylinders, the vortices which form are true Taylor vortices in the sense that each pair of vortices has a fixed wavelength over (most of) the length of the cylinders. However, strictly speaking, once the cylinders become shorter, it is no longer appropriate to describe the formation of Taylor vortices due to the presence of the Ekman circulation, which can cause the wavelength of a pair of vortices to differ along the length of the cylinders; instead, we describe the formation of cells. However, due to the difficulty in knowing exactly when we have the formation of Taylor vortices or the formation of cells, we use the two words "vortices" and "cells" interchangeably throughout this paper.

The aim of this paper is twofold. First, we want to determine whether or not, in the case of a temporally modulated flow, the presence of the ends and the resulting Ekman circulation can prevent the occurrence of reversing or nonreversing flows. Second, we want to explore the very-small-aspect-ratio regime. In this case we examine the effect of a temporal modulation on the selection of the one- and two-cell flow structures that have been observed in the steady case. Essentially we want to determine whether the transition from RTVF to the newly discovered NRTVF depends on the cylinders' finite height in an actual experimental apparatus.

The plan of the paper is the following. Section II contains the governing equations of motion and a brief description of the numerical method. Results are presented in Secs. III and IV. Section III is divided into four parts: low-frequency

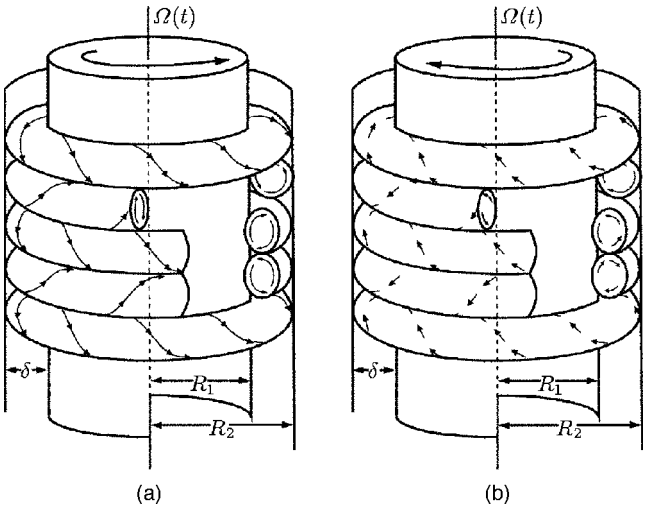

FIG. 1. Schematic of reversing Taylor vortex flow (RTVF). In (a) the inner cylinder rotates in a counterclockwise direction (say, at $t=\tau/4$, where $\tau=2\pi/\omega$ is the period of the forcing and ω is the dimensionless frequency) and the vortices respond by rotating in a particular radial direction; in (b) the inner cylinder rotates in a clockwise direction (say, at $t=3\tau/4$) and the vortices respond by rotating in the opposite radial direction to the first half-cycle.

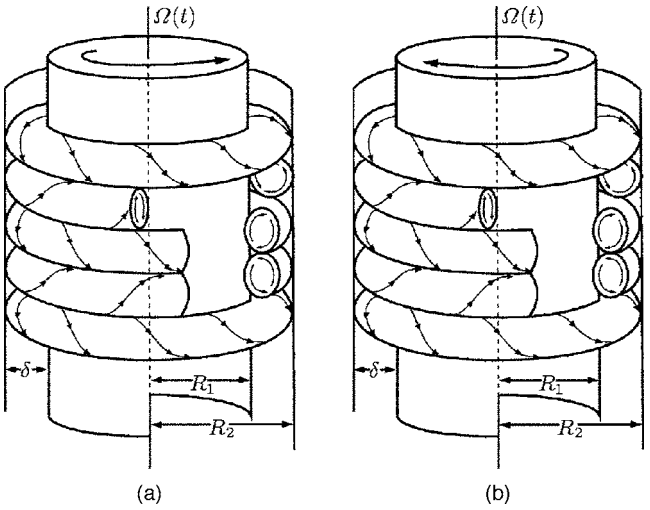

FIG. 2. Schematic of nonreversing Taylor vortex flow (NRTVF). In (a) the situation is as in Fig. 1(a), but in (b), when the cylinder rotates clockwise, the vortices rotate in the same radial direction as in the first half-cycle.

modulation at intermediate aspect ratios (Sec. III A), low-frequency modulation at large aspect ratios (Sec. III B), high-frequency modulation (Sec. III C), and noninteger aspect ratios (Sec. III D). The first part (Sec. III A) is further divided into three subparts devoted, respectively, to small (Sec. III A 1), intermediate (Sec. III A 2), and large (Sec. III A 3) amplitudes of modulation. Section IV is concerned with results at small aspect ratios. Section V contains a final discussion.

II. EQUATIONS, BOUNDARY CONDITIONS, AND FORMULATION

We study the problem using the incompressible Navier-Stokes equations

$$\partial_t \boldsymbol{u} + (\boldsymbol{u}\cdot\boldsymbol{\nabla})\boldsymbol{u} = -\frac{1}{\rho}\boldsymbol{\nabla} p + \nu\nabla^2\boldsymbol{u}, \tag{2}$$

$$\boldsymbol{\nabla}\cdot\boldsymbol{u} = 0, \tag{3}$$

where $\boldsymbol{u}$ is the fluid velocity, p is the pressure, and ν is the (constant) kinematic viscosity. We let R_1 and R_2 be the inner and outer cylinder radii, respectively, and we use cylindrical coordinates (r,θ,z). We nondimensionalize the equations using the gap between the cylinders $\delta=R_2-R_1$ as the length scale and the viscous diffusion time across the gap δ^2/ν as the time scale. The resulting dimensionless parameters are the radius ratio $\eta=R_1/R_2$, the aspect ratio $\Gamma=h/\delta$ (where h is the height of the cylinders) and the imposed amplitude and frequency of modulation, $\mathrm{Re}_{\mathrm{mod}}=\Omega_a\delta R_1/\nu$ and ω; the instantaneous Reynolds number of the inner cylinder is thus

$$\mathrm{Re}(t) = \mathrm{Re}_{\mathrm{mod}}\cos(\omega t). \tag{4}$$

For most of the paper we make the simplifying assumption that the aspect ratio Γ takes only integer values, and so we expect that, for steady rotations of the inner cylinder and quasistatic increase of the Reynolds number, there will be Γ cells within the gap. At the relatively small Reynolds numbers which we consider we expect the flow to be axisymmetric which is consistent with observations of steady Taylor-Couette flow in this range. The governing equations are solved by a finite-difference method using the stream function-vorticity formulation. The equations are discretised using second-order accurate centred differences and are time stepped using a combination of second-order accurate Crank-Nicolson and Adams-Bashforth methods. The Poisson equation for the stream function is solved using parallel SCALAPACK [13] linear algebra routines. An LU (lower-upper) matrix factorization is performed before the time stepping begins since the matrices involved in solving the Poisson equation do not depend on time. This factorization is then used in a call to a solver routine at each time step. Typically, we use time steps of the order of 10^{-4} or 10^{-5} and spatial resolutions of $N_r=40-80$ radial grid points with $N_z=\Gamma N_r$ axial grid points. If the aspect ratio is not integer, we take the number of axial grid points to be the nearest even integer greater than ΓN_r.

The boundary conditions are the familiar no-slip conditions $u_r=u_z=0$ at $r=R_1$ and R_2, $u_\theta=\mathrm{Re}(t)$ at $r=R_1$, and $u_\theta=0$ at $r=R_2$. At the end walls we require $u_r=u_\theta=u_z=0$ at $z=0$ and h.

In an experimental apparatus a small gap must be left between the rotating inner cylinder and the stationary end walls to prevent temperature gradients building up which is what would occur if the boundaries were allowed to meet. This discontinuity creates difficulties in numerical calculations where the azimuthal velocity increases instantaneously from 0 to Re. Due to the difficulties in determining the exact

form of the boundary condition to model this situation, a small parameter $\epsilon \ll 1$ is often used which enables the azimuthal velocity to vary smoothly between the boundary values along the end walls. The works cited in the Introduction have generally used mesh refinement in the corners but it is found that the disturbance caused by the discontinuity does not extend significantly into the fluid provided the mesh size is small enough. Indeed, Lücke *et al.* [14] remarked that no anomalies could be found within a distance of 0.2 mm of the corners of their experimental apparatus with a gap width of $\delta=1.126$ cm. Figure 17 in Sec. IV represents an important test of our code against known results. It shows the boundaries of symmetry-breaking bifurcations of the one- and two-cell flows which we describe in that section. The curves were initially determined experimentally by Benjamin and Mullin [6] and then numerically by Cliffe [7] (at $\eta=0.615$) and Pfister *et al.* [8] (at $\eta=0.5$, who also determined time-dependent boundaries). Due to the small values of the aspect ratio in the figure, the critical Reynolds numbers for the onset or disappearance of new flow patterns could be particularly sensitive to the effects of the discontinuity in the corners. To graphical accuracy, our results (at $\eta=0.5$) compare well with those of Pfister *et al.* [8]. In particular, the hysteresis region given by *BC* in Fig. 17 may be extremely sensitive to experimental errors and numerical inaccuracy; Pfister *et al.* [8] determined the region to be $1.267 \leqslant \Gamma \leqslant 1.304$, and we have determined it to be $1.267 \leqslant \Gamma \leqslant 1.294$. Our results agree well with those of Pfister *et al.* [8]. Furthermore, we tested our code on a finer spatial mesh by increasing the number of radial grid points from 80 to 160. We calculated the critical Reynolds numbers at $\Gamma=0.25$ on the curve *AB* and at $\Gamma=0.97$ on the curve *CD*, where the greatest inaccuracies lie in our code, and found that they are altered by 0.1% with the increase in the number of mesh points. Therefore, in our numerical code we do not implement mesh refinement or give any special treatment to the discontinuity in the corners.

III. RESULTS: REVERSING AND NONREVERSING FLOWS

To make comparisons with the results from the infinite-cylinder approximation we concentrate our attention on the primary flow which develops smoothly from time-dependent Couette flow as the modulation amplitude is increased. Just as in the infinite-cylinder model we can distinguish between low ($\omega \lesssim 4$) and high ($\omega \gtrsim 4$) frequencies, so flows at two different frequencies in the same low- or high-frequency regime undergo the same transitions (but not necessarily at the same Reynolds numbers). Therefore, we consider two frequencies $\omega=3$ (which was classed as low-frequency in our previous papers and is typical of RTVF for $\Gamma \to \infty$) which is representative of flows in the low-frequency regime and $\omega=7$ (which was classed as high frequency and is typical of NRTVF at $\Gamma \to \infty$) which is representative of flows in the high-frequency regime. Note that both frequencies $\omega=3$ and $\omega=7$ are relatively small, in the sense that the (dimensionless) viscous penetration depth of the oscillating flow, $\delta_s=\sqrt{(2/\omega)}$, is of order unity. We do not discuss very high frequencies where δ_s is not of order unity. The radius ratio is $\eta=0.75$.

We shall be predominantly concerned with even aspect ratios where, in the case of steady rotations of the inner cylinder, we would expect there to be an even number of cells which form from the ends and meet symmetrically at the midplane. Some calculations were performed at noneven (and noninteger) aspect ratios and they are described later in Sec. III D. In order to understand the rôle played by the end walls and to make connections to previous results obtained in the infinite-cylinder approximation ($\Gamma \to \infty$), it is convenient to distinguish between intermediate values of aspect ratio ($4 \leqslant \Gamma \leqslant 12$) and large values ($\Gamma \geqslant 14$).

A. Low-frequency modulation, intermediate aspect ratios

We first concentrate on the low-frequency case in which $\omega=3$. We find that for all even aspect ratios $4 \leqslant \Gamma \leqslant 12$ the primary flow is NRTVF. The Taylor vortex cells form near the ends and meet at the midplane. When the flow intensity is at a maximum during a cycle, the number of cells depends on the amplitude of modulation, $\mathrm{Re}_{\mathrm{mod}}$. Figure 3 shows the maximum positive and negative amplitudes of the radial velocity u_r within a cycle at the midpoint (in the middle of the gap at the midplane) versus $\mathrm{Re}_{\mathrm{mod}}$ for a nonreversing flow. Different flow regimes are possible, depending on $\mathrm{Re}_{\mathrm{mod}}$, so we distinguish between small, intermediate, and large amplitudes of modulation.

1. Small amplitude of modulation

To illustrate this regime we choose $\mathrm{Re}_{\mathrm{mod}}=140$ at $\Gamma=8$. Figure 4 shows the radial velocity u_r at the midpoint versus time over a cycle for NRTVF. The period of the forcing is $\tau=2\pi/\omega$, and the flow responds synchronously with a period of $\tau/2$. This is in agreement with the results of our previous papers [1,2] in the infinite-cylinder approximation.

The primary flow developing from oscillating azimuthal flow is a nonreversing flow with an inflow at the midplane. When the cells have fully formed there are $\Gamma=8$ cells within the gap, inflows near the end walls, and, since $\Gamma/2=4$ is even, an inflow at the midplane. Figure 6, below, shows computed contour plots of the stream function for NRTVF at various times over half a cycle with parameters as in Fig. 3 and for $\mathrm{Re}_{\mathrm{mod}}=140$. For the sake of graphical clarity, we do not plot the stream function over the entire range $0 \leqslant z \leqslant \Gamma=8$. The reason for this is that the cells close to the end walls are always visible even at very low rotation rates, so when the radial velocity at the midplane is very small it may be much larger near the end walls. Consequently, using the same number of contour levels over the whole length of the cylinders would either hide the structure close to the midplane as shown in Fig. 5(a) or make the concentration of contours too high near the ends as shown in Fig. 5(b). We choose instead to plot the stream function over $1 \leqslant z \leqslant 7$ only, so that the flow structure near the midplane is fully visible.

In Fig. 6(a) the inner cylinder is rotating in one particular direction with the Reynolds number increasing toward the maximum amplitude. The vortices respond by forming symmetrically from the ends with their own particular rotation direction; in (b) the intensity of the flow at the midplane

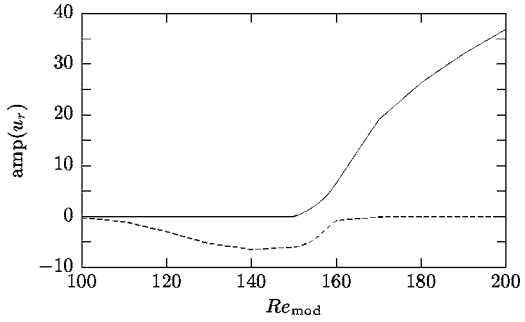

FIG. 3. Maximum positive amplitude (solid line) and maximum negative amplitude (dashed line) of the radial velocity u_r [at the midpoint $r=1+\eta/2(1-\eta)$ and $z=\Gamma/2$] versus amplitude of modulation for $\mathrm{Re}_{\mathrm{mod}}$ NRTVF at $\eta=0.75$, $\Gamma=8$, and $\omega=3$.

increases and in (c) there are eight fully formed vortices within the gap as the modulation amplitude is close to maximum. The remaining figures (d)–(f) show the flow structure as the modulation amplitude decreases toward zero until we are left with only a strong Ekman circulation near to the end walls. Note that for a brief moment during the decay—see (e)—the radial flow at the midplane actually becomes positive, indicating outflow rather than inflow. However, this transient is so short and its amplitude so small—$|u_r| \approx 0.001$ in (e) compared to $|u_r| \approx 6$ in (c). In the second part of the cycle when the inner cylinder rotates in the opposite direction the vortices respond by rotating in the same direction as in the first part of the cycle.

2. Intermediate amplitude of modulation

As the modulation amplitude is further increased, this nonreversing flow undergoes a smooth transition to another flow structure (again with eight fully formed cells) which corresponds to the region of $150 \lesssim \mathrm{Re}_{\mathrm{mod}} \lesssim 160$ in Fig. 3. In this region the maximum positive and negative amplitudes of the radial velocity are of the same order. Figure 7 shows the radial velocity versus time as in Fig. 4 but now for $\mathrm{Re}_{\mathrm{mod}}=155$.

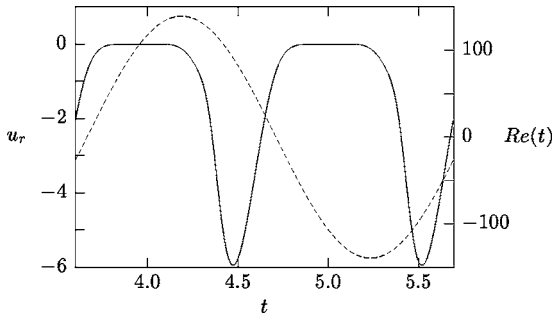

FIG. 4. Radial velocity u_r [at the midpoint $r=1+\eta/2(1-\eta)$ and $z=\Gamma/2$] versus time over a cycle for NRTVF at $\eta=0.75$, $\Gamma=8$, $\omega=3$, and $\mathrm{Re}_{\mathrm{mod}}=140$ (solid line). Also shown (dashed line) is the Reynolds number $\mathrm{Re}(t)$—see vertical axis on the right. In this and subsequent time-series figures, we plot the achieved settled oscillations past the initial transient; t is the time taken from the initial time $t=0$.

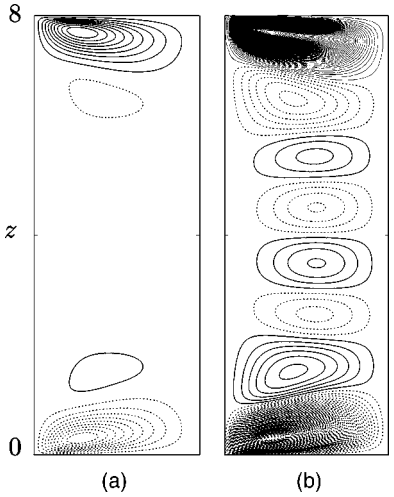

FIG. 5. Computed contour plots of the stream function over the whole length of the cylinder $0 \leqslant z \leqslant 8$ showing the problems presented by the choice of contour levels. In (a) the number of contour levels is chosen so as to capture the structure at the ends, but this hides the structure close to the midplane; in (b) the number of contour levels is chosen so as to show the structure at the midplane, but now the contours are too dense close to the ends.

In contrast to the case where $\mathrm{Re}_{\mathrm{mod}}=140$ the radial velocity changes sign during a cycle, suggesting that this flow is actually a reversing flow. However, this flow again responds to the driving period τ with a period of $\tau/2$. We found in our previous papers that the nonreversing flows always responded to the driving with a period of $\tau/2$ and the reversing flows responded with a period of τ. Figure 7 appears to shows a reversing flow which responds with a period of $\tau/2$.

The true nature of the flow is revealed by contour plots of the stream function at various times within half a cycle as in Fig. 8. The axial extent of the plots is again $1 \leqslant z \leqslant 7$ for clarity. In Fig. 8(a) the Reynolds number of the inner cylinder is increasing and the vortices respond by forming symmetrically from the ends; in (b) the Reynolds number reaches its maximum amplitude within the half-cycle and two new vortices appear from the inner cylinder and attempt to push themselves across the gap. At this point the radial velocity is at its maximal positive amplitude $|u_r| \approx 6$. However, the modulation amplitude is not large enough and, when the Reynolds number begins to decrease (c), these two new vortices are squeezed back out by the stronger vortices that have already formed symmetrically from the ends. At this time of the cycle there are $\Gamma=8$ cells within the gap and the radial velocity achieves its maximum negative amplitude. In (d)–(f) as the Reynolds number decreases within the half-cycle, the vortices decay in the same way as in Fig. 6. In the second part of the cycle the same flow structure emerges. We conclude that the flow is actually a nonreversing flow. The reason for the positive u_r in Fig. 7 for $t \approx 5.4$ and 6.5 is that as the small vortices appear from the inner cylinder, the radial velocity must change sign as the polarity of the small cells is different to the cells that are already closest to the midplane. When the small vortices subsequently disappear, the original polarity of the cells and the sign of the radial velocity are restored.

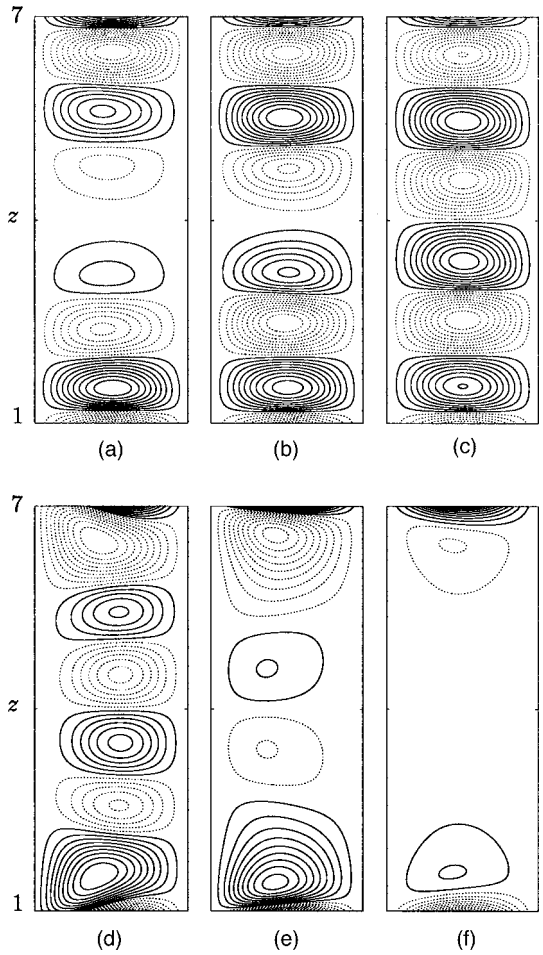

FIG. 6. Computed contours of the stream function for a nonreversing flow at $\Gamma=8$, $\eta=0.75$, $\omega=3$, and $\mathrm{Re}_{\mathrm{mod}}=140$, plotted only for $1\leqslant z\leqslant 7$. When the vortices form, there are $\Gamma=8$ cells within the gap. The flow responds to the driving (period $\tau=2\pi/\omega$) with period $\tau/2$. The times of the snapshots are (a) $t=4.246$ (which corresponds to 0.308τ during a cycle which begins at $t=3.600$), (b) $t=4.318(0.343\tau)$, (c) $t=4.495(0.427\tau)$, (d) $t=4.856(0.600\tau)$, (e) $t=4.887(0.614\tau)$, and (f) $t=4.939(0.639\tau)$. Solid contours represent vortices rotating counterclockwise; dashed contours represent vortices rotating clockwise. The inner cylinder is on the left and the outer cylinder on the right.

3. Large amplitude of modulation

There is a final smooth transition from this flow structure to another state as the modulation amplitude is further increased. This corresponds to the region of $\mathrm{Re}_{\mathrm{mod}}\gtrsim 160$ in Fig. 3. In this case the radial velocity does not change sign within a cycle, but in contrast to the case where $\mathrm{Re}_{\mathrm{mod}}=140$, it increases in the positive direction. The flow again responds with period $\tau/2$. Figure 9 shows the radial velocity at the midpoint versus time over a cycle for this flow at $\mathrm{Re}_{\mathrm{mod}}=180$.

Contour plots of the stream function for $\mathrm{Re}_{\mathrm{mod}}=180$ at various times during a cycle are shown in Fig. 10. The vortices form symmetrically at the end walls as the Reynolds number is increased—see Fig. 10(a)—as in Secs. III A 1 and III A 2. In (b) for $\mathrm{Re}_{\mathrm{mod}}=155$, two new vortices appear from the inner cylinder. However, in contrast to the case $\mathrm{Re}_{\mathrm{mod}}=155$, the modulation amplitude is now large enough that the new small vortices can force their way across the gap and grow to the size of the other vortices. In (c), as the Reynolds number is maximal within the half-cycle, there are now $\Gamma+2=10$ cells within the gap, giving rise to an outflow at the midplane. The vortices then decay in (d)–(f) as the Reynolds number decreases.

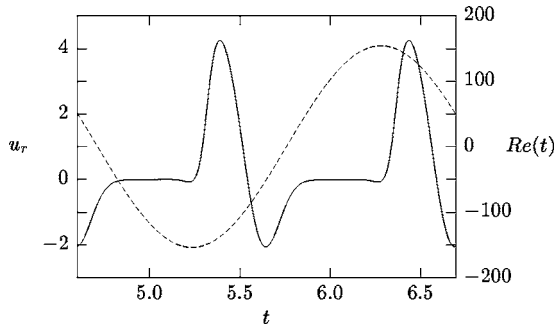

FIG. 7. Radial velocity u_r versus time over a cycle as in Fig. 4 for NRTVF with the same parameters except $\mathrm{Re}_{\mathrm{mod}}=155$.

The scenarios presented above are representative of all the nonreversing flows that are found for even aspect ratios $\Gamma\leqslant 12$ and for low frequency. When $\Gamma/2$ is even, as in the cases above, the primary flow is a nonreversing flow with Γ cells and with an inflow at the midplane. As the modulation amplitude is increased, this flow undergoes a transition to a nonreversing flow with $\Gamma+2$ cells and an outflow at the midplane. When $\Gamma/2$ is odd the primary flow is a nonreversing flow with Γ cells with an outflow at the midplane; then, as the modulation amplitude is increased, the resulting flow is a nonreversing flow with $\Gamma+2$ cells and an inflow at the midplane.

Due to the Ekman circulation induced by the end walls, the bifurcation is imperfect so the transition from oscillating azimuthal flow to cellular vortex flow is smooth. It is therefore impossible to accurately state the critical modulation amplitude for the bifurcation, but it is clear that, as the aspect ratio is increased, the oscillating azimuthal flow becomes more stable and the transition to the cellular state is pushed to higher modulation amplitudes. The region in which the radial velocity is both positive and negative during a cycle is pushed to higher Reynolds numbers as the aspect ratio is decreased.

B. Low-frequency modulation, large aspect ratios

For even aspect ratios $\Gamma\geqslant 14$ at low frequency of modulation, the primary flow is no longer a nonreversing flow but a reversing flow. Figure 11 shows the maximum positive and negative amplitudes of the radial velocity at the midpoint versus modulation amplitude, $\mathrm{Re}_{\mathrm{mod}}$, for a reversing flow at $\Gamma=14$. From this figure it can be seen that the maximum positive and negative amplitudes of the radial velocity are of the same order, although they are not equal and opposite. This is due to the different intensities and sizes of the inflow and outflow jet regions. It is also apparent from the figure that, unlike for intermediate aspect ratios where increasing

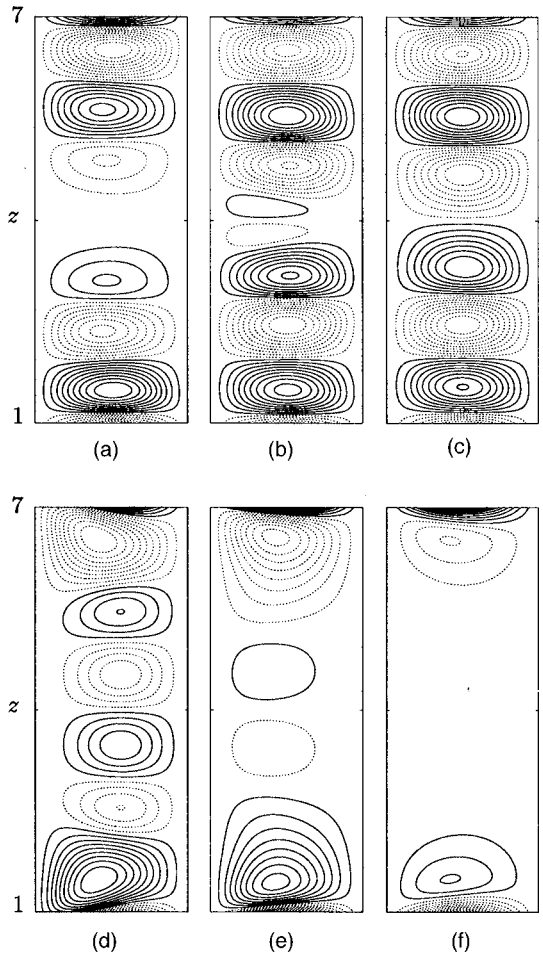

FIG. 8. Computed contours of the stream function for a nonreversing flow at $\Gamma=8$, $\eta=0.75$, $\omega=3$, and $\mathrm{Re}_{\mathrm{mod}}=155$ and for $1\leqslant\Gamma\leqslant 7$. When the vortices form there are $\Gamma=8$ cells within the gap. The flow responds to the driving with period $\tau/2$. The times of the snapshots are (a) $t=5.254$ (which corresponds to 0.312τ during a cycle which begins at $t=4.600$), (b) $t=5.410(0.387\tau)$, (c) $t=5.629(0.491\tau)$, (d) $t=5.906(0.624\tau)$, (e) $t=5.938(0.639\tau)$, and (f) $t=6.042(0.689\tau)$. Solid contours represent vortices rotating counterclockwise; dashed contours represent vortices rotating clockwise. The inner cylinder is on the left and the outer cylinder on the right.

the modulation amplitude gives rise to three different regimes, the flow pattern remains the same for all supercritical modulation amplitudes considered. Figure 12 shows the radial velocity at the midpoint versus time over a full cycle: note that u_r changes sign with $\mathrm{Re}(t)$.

The number of cells that fill the gap now depends on the Reynolds number within a cycle. For the first part of the cycle, when the Reynolds number is positive, there are $\Gamma=14$ cells within the gap; for the second part of the cycle, when the Reynolds number is negative, there are $\Gamma+2=16$ cells within the gap. As for the case of infinite cylinders [1,2], there is a smooth transition between these two states, as a nodal line [the locus of points in the (r,z) plane where $u_r=0$] crosses the gap. This nodal line is well known in the case of steady counterrotating cylinders [15]; however, the nodal line is at a fixed radial position and does not move across the gap. The key difference between the case of finite

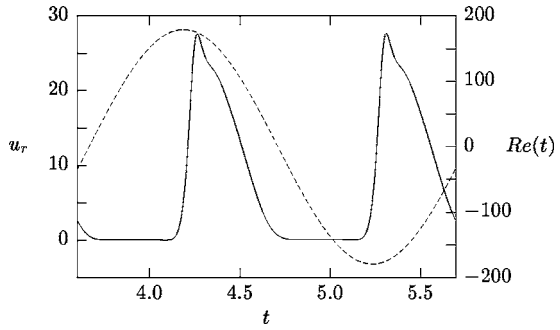

FIG. 9. Radial velocity u_r versus time over a cycle as in Fig. 4 for NRTVF with the same parameters except $\mathrm{Re}_{\mathrm{mod}}=180$.

but large aspect ratio and the limit $\Gamma\to\infty$ is that, for finite Γ, not *all* the vortices reverse their rotation direction. We find that the cells closest to the end walls always rotate in the same direction during a cycle, leaving a reversing flow in a section away from the end walls. Two new cells appear symmetrically about the midplane at the boundary between the reversing and nonreversing cells. This is why there are Γ cells for the first part of the cycle and $\Gamma+2$ cells for the second part.

We illustrate the low-frequency, large-aspect-ratio regime with $\mathrm{Re}_{\mathrm{mod}}=170$ which is representative of the flows found for $\mathrm{Re}_{\mathrm{mod}}\gtrsim 140$. Figure 13 shows contours of the stream function for a reversing flow at $\Gamma=14$ and $\mathrm{Re}_{\mathrm{mod}}=170$ at two different times during a cycle. The contours are shown for $0\leqslant z\leqslant\Gamma/2$ for clarity (the same pattern is found in the upper part of the cylinder). In Fig. 13(a) the Reynolds number is positive and there are $\Gamma=14$ cells within the gap; in (b) the Reynolds number is negative and there are $\Gamma+2=16$ cells within the gap. It can be seen from the figure that the three cells closest to the end walls exhibit no deformation in size with only a slight deformation in the fourth cell. It is in this region that there is no reversal of the cells; for z larger than about 4 the cells are squeezed in the axial direction in the second part of the cycle to allow the extra cells to fit within the gap.

Figure 14 shows, in more detail, the reversing flow during the brief interval in which a reversal takes place in the middle region. The figures are plotted for $3\leqslant z\leqslant 11$ only; outside this region the cells do not undergo the reversal. In Fig. 14(a) there are fully formed vortices which fill the entire gap radially; to follow the reversal process we label the position of the second, third, and fourth cells from either end of the central section $3\leqslant z\leqslant 11$ of the cylinder which is shown with the symbols A, B, and C, respectively. In Fig. 14(a) the cells at A, B, and C are of equal size. In (b) two new cells start to appear near the inner cylinder on either side of the midplane and the B cells are pushed towards the outer cylinder by a "nose" which forms on the A cells. This process continues in (c). In (d) there are now four cells in the regions marked C; a nodal line divides the two cells near the inner cylinder from the cells near the outer cylinder, exactly as in our previous calculations with the infinite-cylinder model. The nodal line moves quickly across the gap, while the cells at B are pushed radially out by the growing cells at A. Finally, in (f) there are now fully formed vortices which extend

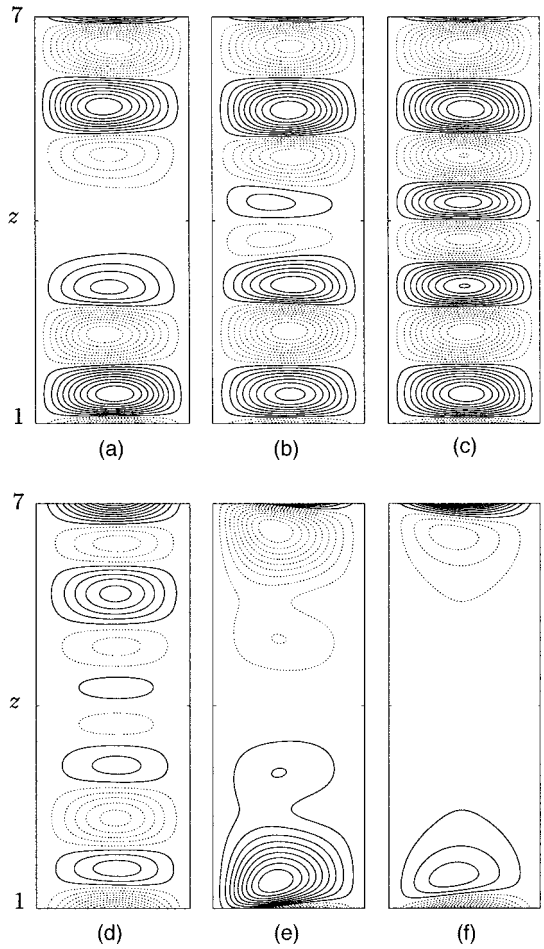

FIG. 10. Computed contours of the stream function for a nonreversing flow at $\Gamma=8$, $\eta=0.75$, $\omega=3$, and $\mathrm{Re}_{\mathrm{mod}}=180$ and for $1\leqslant\Gamma\leqslant 7$. When the vortices form there are $\Gamma+2=10$ cells within the gap. The flow responds to the driving with period $\tau/2$. The times of the snapshots are (a) $t=4.156$ (which corresponds to 0.256τ during a cycle which begins at $t=3.620$), (b) $t=4.198(0.276\tau)$, (c) $t=4.281(0.316\tau)$, (d) $t=4.777(0.552\tau)$, (e) $t=4.870(0.597\tau)$, and (f) $t=4.933(0.627\tau)$. Solid contours represent vortices rotating counterclockwise; dashed contours represent vortices rotating clockwise. The inner cylinder is on the left and the outer cylinder on the right.

across the gap with opposite polarity to those in (a).

The reversal process takes place in a fraction of a diffusion time and the time scale on which it occurs is comparable to the time scale based on the modulation amplitude Ω_a of the inner cylinder. The relation between the time based on the diffusion time scale, t_{diff}, and the time based on the modulation amplitude of the inner cylinder, t_{mod}, is $t_{\mathrm{mod}}=\mathrm{Re}_{\mathrm{mod}}(1-\eta)t_{\mathrm{diff}}/\eta$.

As the aspect ratio is increased, the number of vortices undergoing a complete reversal increases, while the number of vortices close to the ends which do not undergo a reversal remains roughly constant at about 3–5. This is true for all aspect ratios up to the largest we examined at $\Gamma=40$, and at this aspect ratio most of the vortices within the gap are free from the influence of the Ekman circulation.

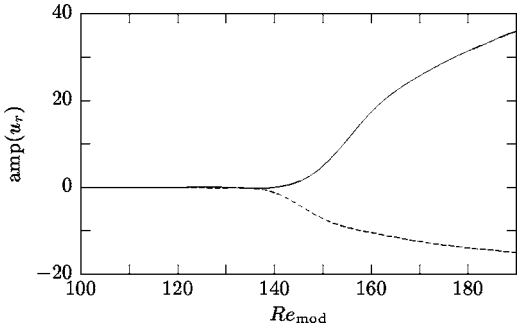

FIG. 11. Maximum positive amplitude (solid line) and maximum negative amplitude (dashed line) of the radial velocity u_r [measured at $r=1+\eta/2(1-\eta)$ and $z=\Gamma/2$] versus amplitude of modulation $\mathrm{Re}_{\mathrm{mod}}$ for RTVF at $\eta=0.75$, $\Gamma=14$, and $\omega=3$.

C. High frequency of modulation

At the higher frequency of $\omega=7$ there is no evidence of any reversing flow for all aspect ratios considered, $4\leqslant\Gamma\leqslant 40$. This is in agreement with the infinite-cylinder model where only nonreversing flows were found at higher frequencies. The only interesting feature of the high-frequency case is the number of cells that are formed when the Reynolds number is supercritical. For even aspect ratios $4\leqslant\Gamma\leqslant 8$ the primary flow is a nonreversing flow with Γ cells but for $\Gamma\geqslant 10$ the primary flow is a nonreversing flow with $\Gamma+2$ cells. As in the low-frequency case, these nonreversing flows respond to the driving with period $\tau/2$.

In the high-frequency case it is straightforward to find a secondary disconnected flow. To begin with, a flow on the primary branch is found with modulation amplitude $+\mathrm{Re}_{\mathrm{mod}}$; for $4\leqslant\Gamma\leqslant 8$ this flow has Γ cells, and for $\Gamma\geqslant 10$ it has $\Gamma+2$ cells. Then, within the cycle, the sign of the modulation amplitude is instantaneously switched to $-\mathrm{Re}_{\mathrm{mod}}$. This corresponds to an instantaneous change of rotation direction of the inner cylinder. The resulting flow is on the disconnected branch of the bifurcation and for $4\leqslant\Gamma\leqslant 8$ this flow has $\Gamma+2$ cells, whereas for $\Gamma\geqslant 10$ it has $\Gamma+4$ cells. All these flows respond to the driving with period $\tau/2$.

D. Noninteger, noneven aspect ratios

Some calculations have been done to determine the transition between flows as the aspect ratio is increased but the modulation amplitude is fixed.

For intermediate aspect ratios and low frequencies the flow patterns observed are qualitatively similar to those when fixing the aspect ratio and varying the modulation amplitude as in Figs. 6, 8, and 10. If we let Γ_1 and $\Gamma_2>\Gamma_1$ be two consecutive even aspect ratios (and for not too large modulation amplitude), then when $\Gamma=\Gamma_1$ the primary flow consists of Γ_1 cells and when $\Gamma=\Gamma_2$ the primary flow consists of Γ_2 cells. These flows are nonreversing flows. As the aspect ratio is increased from Γ_1 to Γ_2 two new cells start to appear from the inner cylinder just as in the case of intermediate amplitude of modulation with fixed aspect ratio (Fig. 8). When the aspect ratio is not large enough these two new cells are squeezed back out by the existing cells, leaving a flow with Γ_1 cells; however, when the aspect ratio is larger

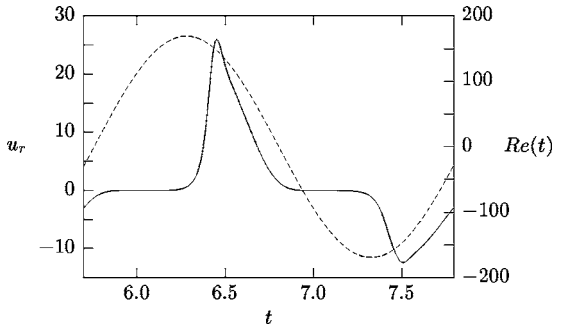

FIG. 12. Radial velocity u_r versus time over a cycle as in Fig. 4 for RTVF with the same parameters except $\Gamma=14$ and $\mathrm{Re}_{\mathrm{mod}}=170$. The flow responds synchronously to the driving with a period of τ.

these two new cells are able to extend across the gap and grow to the size of the existing vortices leaving a flow with Γ_2 cells (Fig. 10). This is a smooth process as the aspect ratio is increased, and there is no definite aspect ratio at which the two new cells appear. The same process occurs for higher modulation amplitudes where the flow consists of $\Gamma+2$ cells.

For larger aspect ratios and low frequencies a slightly different transition takes place as the aspect ratio is increased from Γ_1 to Γ_2. When $\Gamma=\Gamma_1$ the flow is reversing with Γ_1 cells in the first part of the cycle and Γ_1+2 cells in the second part of the cycle. As the aspect ratio is increased toward Γ_2 the flow is still reversing but now has Γ_2 cells in the first part of the cycle and Γ_2+2 cells in the second part of the cycle. Describing the transition as the aspect ratio is increased is most easily undertaken using an example and with reference to Fig. 15 where $\Gamma=15$, $\mathrm{Re}_{\mathrm{mod}}=150$, and $\omega=3$. Let $\Gamma_1=14$ and $\Gamma_2=16$; then, when $\Gamma=14$ there are 14 cells in the first part of the cycle and 16 in the second part of the cycle; when $\Gamma=16$ there are 16 cells in the first part of the cycle and 18 in the second part of the cycle. If the aspect ratio is increased but is not large enough, then there is still an oscillation of 14 and 16 cells within the cycle. If the aspect ratio is further increased, 18 cells try to fit in the gap, creating an oscillation between 16 and 18 cells. This attempt is seen as two new cells appearing from the inner cylinder as in Fig. 15(a) but not at the midplane—the two new cells try to fit in two cells away from the midplane and they are incredibly compressed in the axial direction. Figure 15(b) shows the two new cells pushing further across the gap. However, if the aspect ratio is still not large enough, these two new cells are squeezed out [Fig. 15(c)] and the two cells that were either side of them coalesce to form a new cell, leaving 14 cells in the gap [Figs. 15(d)–15(f)]. Once the aspect ratio is large enough, the two new cells are robust enough to survive and the flow does indeed show an oscillation between 16 and 18 cells. Just as for intermediate aspect ratios this is also a smooth process and there is no definite aspect ratio where the oscillation can be seen to be between 16 and 18 cells rather than between 14 and 16.

The picture is not so clear for aspect ratios in the range $12<\Gamma<14$. In this range of aspect ratios it is very difficult to obtain critical modulation amplitudes and/or aspect ratios for transitions between reversing and nonreversing flows and also for transitions of flows with different numbers of cells.

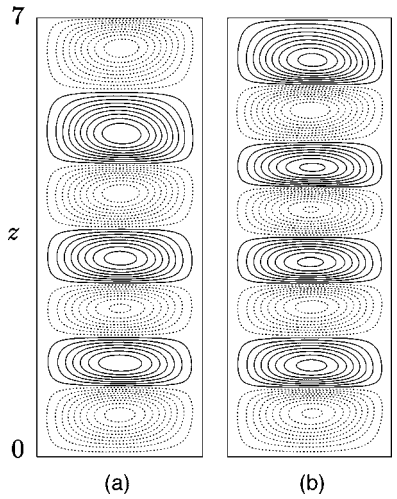

FIG. 13. Computed contours of the stream function for a reversing flow at $\Gamma=14$, $\eta=0.75$, $\omega=3$, and $\mathrm{Re}_{\mathrm{mod}}=170$, plotted in the region $0\leqslant z\leqslant 7$ only. When the vortices form there are (a) $\Gamma=14$ cells within the gap in the first part of the cycle and (b) $\Gamma+2=16$ cells in the second part of the cycle. The flow responds to the driving with period τ. Solid contours represent vortices rotating counterclockwise; dashed contours represent vortices rotating clockwise. The inner cylinder is on the left and the outer cylinder on the right.

The main reason for this is that there is now competition between the reversing and nonreversing flows. However, some progress has been made in determining a general picture of the transitions. For most of the range the primary flow is a nonreversing flow which initially has 12 cells but which undergoes a smooth transition to 14 cells as the modulation amplitude is increased (just as in the intermediate aspect ratio regime $\Gamma\leqslant 12$). However, a sufficient discontinuous jump in the modulation amplitude close to the critical region for the onset of the primary flow causes the flow to become a reversing flow with an oscillation between 14 and 16 cells (just as in the large aspect ratio regime $\Gamma\geqslant 14$). For example, at $\Gamma=13$ the nonreversing flow is the primary flow at $\mathrm{Re}_{\mathrm{mod}}\approx 140$. If the modulation amplitude is increased suddenly to 147, the flow remains as a nonreversing flow; however, if the modulation amplitude is increased suddenly from 140 to 148, the flow is a reversing flow.

When the frequency is higher, the reversing flows no longer exist and the transitions between nonreversing flows as the aspect ratio is increased are the same as for the low-frequency case.

IV. RESULTS: VERY SMALL ASPECT RATIO

Now we turn our attention to the case where the height of the cylinders is of the order of the gap width (and Γ is no longer restricted to being an integer). In this regime reversing and nonreversing flows do not exist and we no longer discuss transitions between them. In the case of steady rotations of the inner cylinder and fixed outer cylinder, a wide variety of flows have been discovered including axisymmetric time-dependent and "side-by-side" flows, depending on

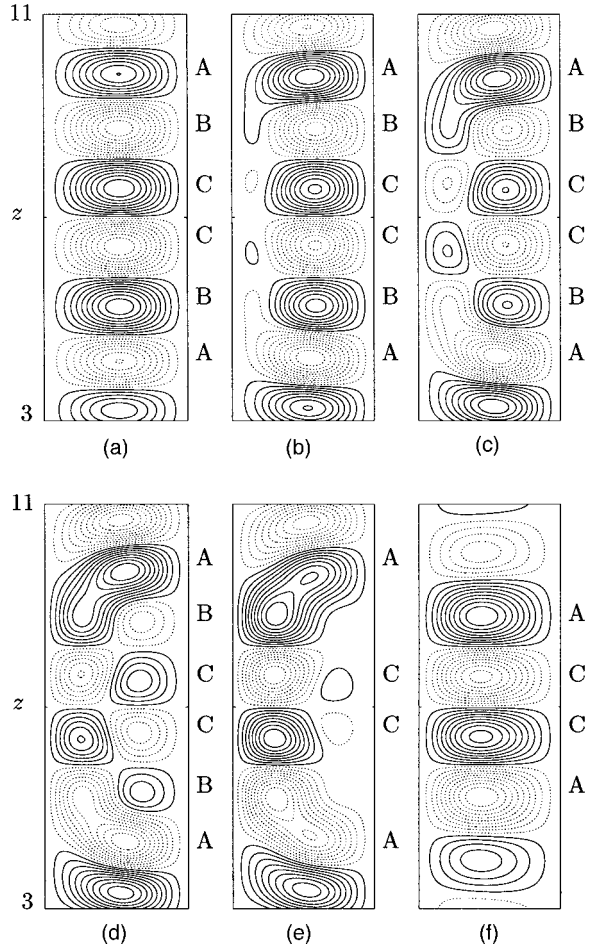

FIG. 14. Computed contours of the stream function for a reversing flow at $\Gamma=14$, $\eta=0.75$, $\omega=3$, and $\mathrm{Re}_{\mathrm{mod}}=170$, plotted in $3\leqslant z\leqslant 11$ only as the reversal process takes place. The flow responds to the driving with period τ. The times of the snapshots are (a) $t=6.916$ (which corresponds to 0.581τ during a cycle which begins at $t=5.700$), (b) $t=6.956(0.600\tau)$, (c) $t=6.962(0.603\tau)$, (d) $t=6.966(0.604\tau)$, (e) $t=6.970(0.606\tau)$, and (f) $t=7.006(0.624\tau)$. Solid contours represent vortices rotating counterclockwise; dashed contours represent vortices rotating clockwise. The inner cylinder is on the left and the outer cylinder on the right. Note how the *B* cells are pushed radially out until they disappear.

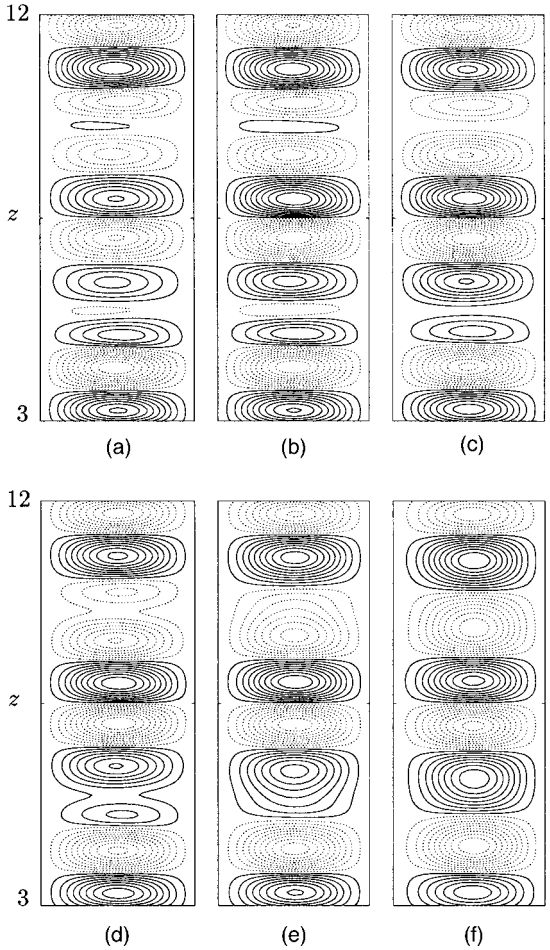

FIG. 15. Computed contours of the stream function showing the appearance of extra cells in the second part of the cycle of a reversing flow with noneven aspect ratio $\Gamma=15$, $\mathrm{Re}_{\mathrm{mod}}=150$, and $\omega=3$. The appearance of the extra cells means that 18 cells try to fit in the gap, but the aspect ratio is not large enough and they are squeezed out leaving 14 cells. The flow responds to the driving with period τ. The times of the snapshots are (a) $t=12.812$ (which corresponds to 0.497τ during a cycle which begins at $t=11.771$), (b) $t=12.874(0.527\tau)$, (c) $t=12.979(0.577\tau)$, (d) $t=13.000(0.587\tau)$, (e) $t=13.104(0.636\tau)$, and (f) $t=13.209(0.687\tau)$.

the route taken through parameter space. The final flow pattern can depend strongly on sudden starts of the cylinder or discontinuous jumps of the aspect ratio. For sufficiently small Reynolds numbers the basic flow is a symmetric two-cell state composing of an Ekman circulation induced by the ends. For a large range of aspect ratios the bifurcation from this two-cell state is to an asymmetric one-cell flow comprising one large cell with a smaller one in the corner next to the inner cylinder. Figure 16 shows these two flow patterns at the same parameters; only the route taken through parameter space to arrive at these states is different. The different flow patterns as a function of Reynolds number Re and aspect ratio Γ were first determined experimentally by Benjamin and Mullin [6] and then numerically by Cliffe [7] (at radius ratio $\eta=0.615$) and later by Pfister *et al.* [8] at $\eta=0.5$. For the rest of this paper we consider a radius ratio of $\eta=0.5$.

Figure 17 shows the region of parameter space examined by Pfister *et al.* [8] for steady rotations which is relevant to our investigation of modulated flows. There are also time-dependent flows in this region (which we do not show in the figure), which we have found in agreement with Pfister *et al.* [8]. We have recomputed all stability curves shown in Fig. 17 for testing purposes, and our results agree with theirs to graphical accuracy. The figure shows the interaction between one- and two-cell flows. The curve *ABCD* corresponds to a symmetry-breaking bifurcation leading to the onset of the asymmetric one-cell state. The arrows (up or down) in the figure represent whether the boundary is found by a quasi-static increase or decrease in the Reynolds number. In the region *BC* (see inset) there is hysteresis between the one- and two-cell states. In the region *CE* the one-cell flow is no longer realizable by a smooth increase of the Reynolds number; this boundary can only be found by, for example, a

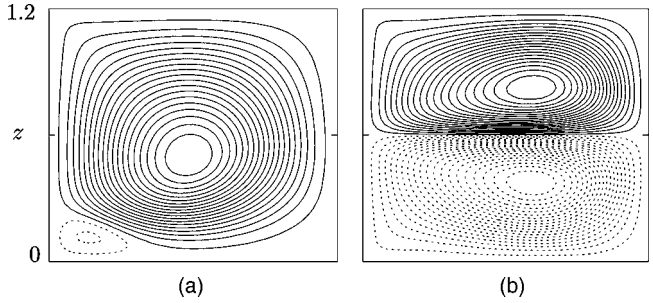

FIG. 16. Computed contours of the stream function of the (a) one-cell and (b) two-cell flows at $\Gamma=1.2$, $\eta=0.5$, and $\mathrm{Re}=400$. Solid lines represent vortices rotating counterclockwise; dashed lines represent vortices rotating clockwise. The inner cylinder is on the left, the outer cylinder on the right.

sudden start of the cylinder or by a jump in aspect ratio from the region inside *ABCD* to outside and above *CE*.

If the inner cylinder does not rotate at constant angular velocity but is modulated as in Eq. (1), a direct comparison with Fig. 17 is not possible. The reason is that there is no equivalent to a sudden start of the cylinder—the time-dependent Reynolds number changes smoothly during a cycle. We should not expect to be able to find boundaries such as *CD* or *CE*, which are realized by sudden jumps in Reynolds number above the boundaries in the steady case.

At subcritical modulation amplitudes the basic flow is a symmetric two-cell flow, similar to the steady case as shown in Fig. 16(b). The only effect of the modulation is to cause a slight deformation of the cells and to make the vortex cores shift slightly during the cycle. The midplane region is always an outflow (the cells do not switch sign).

As in the steady case, the bifurcation from the oscillatory two-cell flow is to an asymmetric state with nonzero axial velocity at the midplane. For various modulation frequencies ranging from $\omega=3$ to $\omega=50$ we have found that the onset of the asymmetric state is smooth as the modulation amplitude is increased. Only when the modulation amplitude is large enough can a definite asymmetric flow pattern be recognized; an example is shown in Fig. 18, where $\Gamma=1$, $\omega=4$, and $\mathrm{Re}_{\mathrm{mod}}=400$.

Over the period $\tau/2$ (where τ is the period of the forcing) an oscillation between the two states shown in Fig. 16 occurs. The flow responds to the driving with period $\tau/2$. When the time-dependent Reynolds number is less than the critical modulation amplitude, the flow is a symmetric two-cell state, but when it is greater than critical the flow is an asymmetric one-cell state, with a smooth transition between the two states.

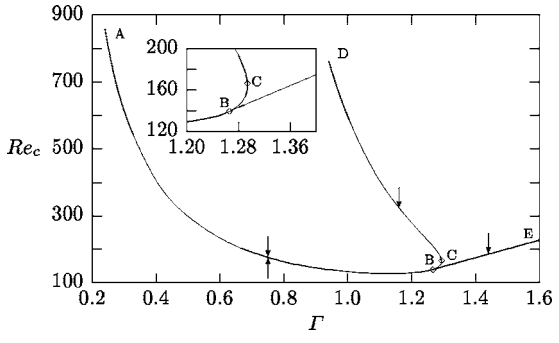

FIG. 17. Critical steady Reynolds number Re_c versus aspect ratio Γ for the transition between one- and two-cell flows for $\eta=0.5$. The arrows denote whether the boundaries can be found by a quasistatic increase (↑) or decrease (↓) of the Reynolds number. The inset is an enlargement of the hysteresis region.

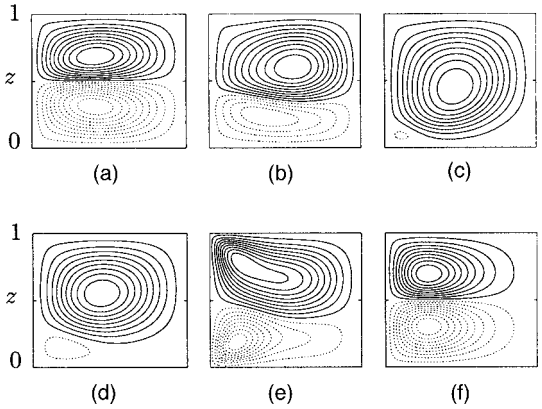

FIG. 18. Computed contours of the stream function for the oscillation between one- and two-cell flows at $\Gamma=1$, $\eta=0.5$, $\omega=4$, and $\mathrm{Re}_{\mathrm{mod}}=400$. The times of the snapshots are (a) $t=17.059$ (which corresponds to 0.006τ during a cycle which begins at $t=17.050$), (b) $t=17.355(0.194\tau)$, (c) $t=17.433(0.244\tau)$, (d) $t=17.612(0.358\tau)$, (e) $t=17.729(0.432\tau)$, and (f) $t=17.807(0.482\tau)$. Solid contours represent vortices rotating counterclockwise; dashed contours represent vortices rotating clockwise. The inner cylinder is on the left and the outer cylinder on the right.

As the modulation frequency is increased significantly the flow has less time to oscillate fully between the symmetric and asymmetric states, and so for larger frequencies the flow remains in an asymmetric state as in Fig. 16(a) with slight deformations of the cells and movement of the vortex cores.

Although it is not possible to accurately calculate the critical modulation amplitude of the onset of this asymmetry, it is clear that the modulation has a stabilizing effect and so the symmetry-breaking bifurcation occurs at larger Reynolds numbers than in the steady case.

We have also found that, as expected, in the range of aspect ratios given by CE in Fig. 17 there is no symmetry-breaking bifurcation and the flow pattern remains as a two-cell symmetric state.

Further exploration of the parameter space has revealed the existence of an oscillating "side-by-side" flow where the cells are positioned radially instead of axially. In the steady case Pfister *et al.* [8] mention observing a "side-by-side two-cell state" at a Reynolds number of $\mathrm{Re}=2000$ and aspect ratio of $\Gamma=0.68$. This state was later confirmed to exist by Furukawa *et al.* [11] in a region of parameter space given by approximately $0.6\lesssim\Gamma\lesssim0.9$ and $700\lesssim\mathrm{Re}\lesssim1400$; the radius ratio in this case was $\eta=0.667$. We have found this flow to exist at $\Gamma=0.7$, $\omega=3$, and $\mathrm{Re}_{\mathrm{mod}}=1500$. Contour plots are shown in Fig. 19. When the time-dependent Reynolds number is supercritical the flow pattern has the side-by-side structure as in the steady case, where the two cells are positioned radially instead of axially; there is still a small vortex in the corner next to the inner cylinder. When the Reynolds number is subcritical, the flow has the familiar two-cell sym-

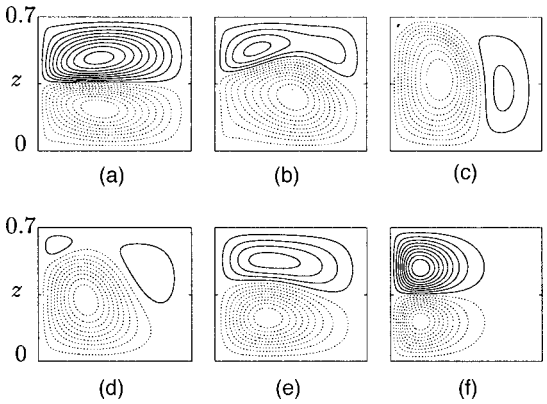

FIG. 19. Computed contours of the stream function for the oscillating "side-by-side" flow at $\Gamma=0.7$, $\eta=0.5$, $\omega=3$, and $\mathrm{Re}_{\mathrm{mod}}=1500$. The times of the snapshots are (a) $t=12.177$ (which corresponds to 0.207τ during a cycle which begins at $t=11.743$), (b) $t=12.239(0.237\tau)$, (c) $t=12.721(0.467\tau)$, (d) $t=13.025(0.612\tau)$, (e) $t=13.088(0.642\tau)$, and (f) $t=13.161(0.677\tau)$. Solid contours represent vortices rotating counterclockwise; dashed contours represent vortices rotating clockwise. The inner cylinder is on the left and the outer cylinder on the right.

metric pattern. As in the oscillation of the one- and two-cell patterns the side-by-side flow responds to the driving with period $\tau/2$. The process by which the radially positioned cells appear is as follows: in Fig. 19(a) the Reynolds number is subcritical within the cycle and we have a two-cell state. As the Reynolds number increases in (b) the lower (clockwise rotating) cell begins to split the upper (counterclockwise rotating) cell; in (c) as the Reynolds number is close to maximal the upper cell has been split in two, with one part forming the small cell close to the inner cylinder and the other part forming a second radial cell. This process is reversed in (d)–(f) as the Reynolds number becomes subcritical within the cycle. The whole process is then repeated in the second half of the cycle.

We have also found a very similar side-by-side flow structure which responds to the driving with a period τ at the same parameters as in the previous case except at a slightly higher frequency of $\omega=4$. For the first part of the cycle the flow pattern is exactly as in Fig. 19. However, in the second part of the cycle, it is the upper (counterclockwise rotating) cell which splits the lower (clockwise rotating) cell so that, whereas in Fig. 19(c) the small cell is in the upper-left corner of the cylinder, it is now in the lower-left corner of the cylinder, and the polarity of the two large radial cells is switched.

V. CONCLUSIONS

The initial motivation of this work was to determine if nonreversing flow solutions of the Navier-Stokes equations, found between infinitely long cylinders [1,2], exist in an experimentally realistic geometry which includes the top and bottom ends. We have found that not only is the answer positive, but nonreversing flows are actually favoured, unless the aspect ratio is rather large. In this case—see Sec. III B—we recover results known from the infinite cylinder approximation.

We have also examined the very small aspect regime and revealed a large variety of flow patterns which are induced by the Ekman circulation, including side-by-side vortices.

It would be interesting to examine the effects of tapered cylinders on the reversing and nonreversing flows (as studied, for example, by Ning *et al.* [16] for steady flows) where the Reynolds number is subcritical in a region near the top and bottom ends.

[1] A. J. Youd, A. P. Willis, and C. F. Barenghi, J. Fluid Mech. **487**, 367 (2003).
[2] A. J. Youd, A. P. Willis, and C. F. Barenghi, Fluid Dyn. Res. **36**, 61 (2005).
[3] P. Zhang, Ph.D. thesis, University of Exeter, 2002.
[4] T. B. Benjamin, Proc. R. Soc. London, Ser. A **359**, 1 (1978).
[5] T. B. Benjamin, Proc. R. Soc. London, Ser. A **359**, 27 (1978).
[6] T. B. Benjamin and T. Mullin, Proc. R. Soc. London, Ser. A **377**, 221 (1981).
[7] K. A. Cliffe, J. Fluid Mech. **135**, 219 (1983).
[8] G. Pfister, H. Schmidt, K. A. Cliffe, and T. Mullin, J. Fluid Mech. **191**, 1 (1988).
[9] K. A. Cliffe, J. J. Kobine, and T. Mullin, Proc. R. Soc. London, Ser. A **439**, 341 (1992).
[10] T. Mullin, Y. Toya, and S. J. Tavener, Phys. Fluids **14**, 2778 (2002).
[11] H. Furukawa, T. Watanabe, Y. Toya, and I. Nakamura, Phys. Rev. E **65**, 036306 (2002).
[12] J. M. Lopez and F. Marques, Phys. Rev. E **68**, 036302 (2003).
[13] L. S. Blackford *et al.*, *ScaLAPACK Users' Guide* (Society for Industrial and Applied Mathematics, Philadelphia, PA, 1997).
[14] M. Lücke, M. Mihelcic, K. Wingerath, and G. Pfister, J. Fluid Mech. **140**, 343 (1984).
[15] S. Chandrasekhar, *Hydrodynamic and Hydromagnetic Stability* (Clarendon, Oxford, 1961).
[16] L. Ning, G. Ahlers, and D. S. Cannell, Phys. Rev. Lett. **64**, 1235 (1990).